Automated Chemical Analysis of Internally Mixed Aerosol Particles Using X-ray Spectromicroscopy at the Carbon K-Edge

Ryan C. Moffet,[1] Tobias Henn,[2] Alexander Laskin,[3] Mary K. Gilles[1*]*

[1]Chemical Sciences Division, Lawrence Berkeley National Laboratory,

Berkeley, California, 94720-8226

[2]Department of Physics, University of Würzburg, Am Hubland, 97074 Würzburg, Germany

[3]W. R. Wiley Environmental Molecular Sciences Laboratory,

Pacific Northwest National Laboratory, Richland, Washington, 99352.

*co-corresponding authors: mkgilles@lbl.gov, Alexander.laskin@pnl.gov

RECEIVED DATE

Abstract.

We have developed an automated data analysis method for atmospheric particles using scanning transmission X-ray microscopy coupled with near edge X-ray fine structure spectroscopy (STXM/NEXAFS). This method is applied to complex internally mixed submicron particles containing organic and inorganic material. Several algorithms were developed to exploit NEXAFS spectral features in the energy range from 278-320 eV for quantitative mapping of the spatial distribution of elemental carbon, organic carbon, potassium, and non-carbonaceous elements in particles of mixed composition. This energy range encompasses the carbon K-edge and potassium L2 and L3 edges. STXM/NEXAFS maps of different chemical components were complemented with a subsequent analysis using elemental maps obtained by scanning electron microscopy coupled with energy dispersive X-ray analysis (SEM/EDX). We demonstrate application of the automated mapping algorithms for data analysis and the statistical classification of particles.

KEYWORDS. STXM/NEXAFS, NEXAFS, SEM/EDX, CCSEM/EDX, CCSEM, Aerosol, Atmospheric, Carbon, K-Edge, Mixing State, Internally Mixed, Molecular Imaging

Introduction

Aerosol particles have a strong impact on a number of environmental fields including climate change, public health, and atmospheric visibility.[1-3] The magnitude of the aerosol effect on these issues is highly uncertain due to an incomplete understanding of their chemical and physical properties. Atmospheric aerosols have a wide range of sizes, sources, and physicochemical properties. Knowledge of these properties is crucial for understanding aerosol effects, origin, and atmospheric history. However, the chemical characterization of environmental particles presents a significant analytical challenge due to their sub-micrometer size and chemical complexity. With the ability to probe the chemistry of individual particles, modern micro-analytical techniques such as microscopy[4] and micro-spectroscopy[5] are instrumental for overcoming these challenges.

Over the last 40 years, electron beam techniques have been increasingly used to characterize individual particles collected in both laboratory and field settings.[6-9] Scanning electron microscopy coupled with energy dispersive X-ray analysis (SEM/EDX) yields images with ~10 nm lateral resolution and EDX provides elemental analysis. Transmission electron microscopy (TEM) coupled with EDX, selected area electron diffraction (SAED) analysis, or electron energy loss spectroscopy (EELS) is extensively used for particle analysis. TEM spatial resolution is higher than SEM, and SAED can provide crystalline structures. While electron beam microscopy methods have the advantage of exquisite spatial resolution, their elemental analysis is not sufficient to characterize carbonaceous aerosol. Ideally, chemical characterization of carbonaceous particles would employ molecular structure information, or at a minimum, speciation of carbon bonding and/or organic functional groups.

Recently, researchers have pushed the abilities of infrared (IR) and Raman micro-spectroscopy techniques to measure the integrated chemical composition of particle ensembles.[10-14] Although vibrational IR and/or Raman micro-spectroscopy can be non-destructive techniques that provide organic functional group information, their spatial resolution is generally insufficient for single submicron particles. This is due to the inability to focus light beams below the diffraction limit[15] and low signal levels afforded by a single submicron particle.[16,17] Within individual particles, the spatial distribution of

chemical compounds affects their chemical and physical properties which in turn affects their environmental impact. Knowledge of spatially resolved chemical composition also aids in deciphering particle aging mechanisms and sources.[18,19] Therefore, developing methodologies that accurately map the internal heterogeneity of individual particles with appropriate statistical depth is important.

The initial application of STXM to field collected aerosols mapped different organic functional groups on a limited number of particles.[20] The number of particles examined was limited both by the experimental time available for data acquisition as well as development of appropriate analytical methods. Over the past decade, STXM has grown into an active area of research examining topics such as the graphitic nature of combustion produced aerosols,[21-23] organic particle speciation,[20] the evolution of aerosol mixing states,[19] and chemical speciation of metal containing aerosols.[24,25] Relating the detailed analysis of a limited number of particles to the larger, more encompassing statistically representative picture has been one of the challenges of this method. Some studies have done this by combining STXM methods with collocated field measurements and complementary electron microscopies.[19,23,26] This allows the STXM data to be placed within a framework of single particle data on tens of thousands of particles to millions of particles. Alternatively, STXM results are placed within the context of complementary bulk information on FTIR, aerosol mass spectrometry or elemental analysis.[27,28] As access to STXM instruments increases and the method becomes more widely applied, improved methods of systematic analysis for a statistically significant number of particles are essential.

This manuscript describes a STXM analytical method for spatially mapping the chemical constituents commonly identified within individual particles: organic carbon, elemental carbon, and inorganic species. We present a software assisted methodology for examining the distribution of these three major components within individual particles. We illustrate how information on non-carbonaceous elements at the carbon K-edge can be obtained. Using the combined detection of non-carbonaceous inorganic species, organic carbon, and elemental carbon we generate component maps of individual particles that can be used for particle-type classification over a large number of particles. The assignment of different chemical constituents within individual particles is confirmed with SEM/EDX elemental maps. One

major advantage of this method is that its simplicity allows for a straightforward interpretation and consistent application across different samples. When applied to multiple datasets, a quantitative statistical comparison between different particle samples can be obtained. As the reliability and throughput of STXM instruments increases, there is greater need for methods to perform fast statistical data analysis for a large number of particles. Additional features can easily be added or changed depending on the characteristics of a particular sample. This analytical framework is applicable to a variety of environmental samples other than atmospheric particles; examples include: soils, meteorites and interplanetary dust, and nanoparticles.

Methods

Particle samples. Samples of airborne particles were collected by impaction using a time resolve aerosol collector (TRAC).[29] Substrates of either Si_3N_4 film supported by a silicon wafer (0.5 × 0.5 mm Si_3N_4 window size, 100 nm Si_3N_4 membrane thickness, 5 × 5 mm Si frame size; Silson, Inc.) or filmed TEM grids (Carbon type B film, Copper 400 mesh grids; Ted Pella, Inc.) were used as impaction substrates. The particle samples were collected in Mexico City during the MILAGRO 2006 campaign at the T0 sampling site.[19,24] Sea salt particles were generated from a 40 g/L aqueous solution prepared from sea salts (Sigma Aldrich) and 18.0 MΩ Milli-Q water. The salt solution was atomized using a flow of nitrogen and particles were sampled using an inertial impactor onto silicon nitride films as described above.

STXM Measurements. The STXM instruments used in this study are located at the Advanced Light Source at Lawrence Berkley National Laboratory. However, the analysis techniques presented here are applicable at the majority of STXMs operating throughout the world as they employ the identical data acquisition software. The design principle of the STXM instrument has been described in detail elsewhere.[30] The basic components of the STXM instrument are shown in Figure 1A. The monochromatic soft X-ray beam produced at the synchrotron source is focused by a Fresnel zone plate to a spot size between 20 and 40 nm, depending upon the zone plate used. The sample is held at the focal point of the monochromatic X-ray beam and raster scanned to obtain an image. X-rays transmitted

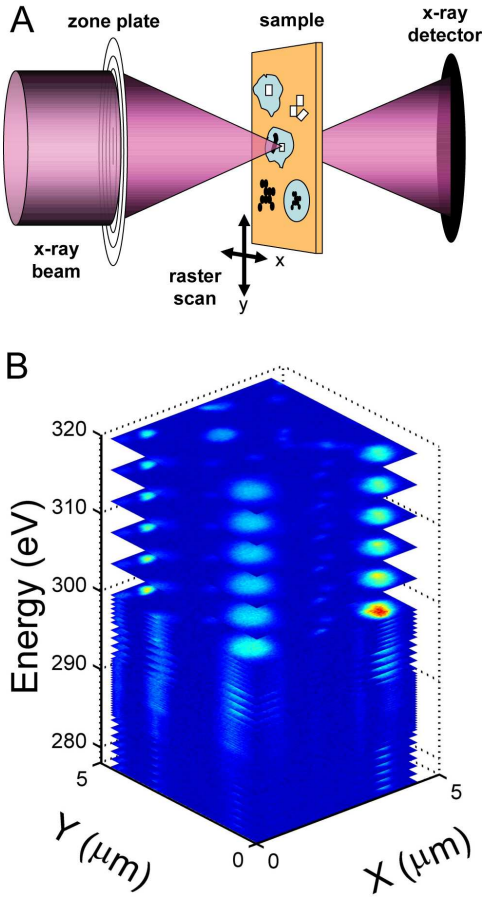

Figure 1. Schematic of the STXM instrument: (A) – basic operation and measurement diagram, (B) - a spectral "stack" of images collected for a single field-of-view of the analyzed sample.

through the sample are detected by a thin layer of phosphor coating on a Lucite light pipe coupled to a photodiode. After an image is collected at a fixed energy, the energy is changed and the sample is scanned again. This process continues for ~100 unevenly spaced energy steps and results in a "stack" of images as demonstrated in Figure 1B. The energy steps are typically smaller in the near edge energy range (285 – 294 eV) to capture narrow spectral features present in that region.

SEM/EDX measurements. A FEI XL30 digital field emission gun environmental SEM located at Environmental Molecular Sciences Laboratory of Pacific Northwest National Laboratory was used for SEM/EDX analysis. The system is equipped with Genesis hardware and software (EDAX, Inc.) for X-ray microanalysis and elemental mapping. The EDX spectrometer has a Si(Li) detector with an active area of 30 mm^2 and ATW2 window, which allows X-ray detection from elements higher than beryllium ($Z > 4$). The X-ray maps were acquired at 10,000× magnification, with 512 × 400 pixel map resolution, a beam current of ~500 pA, and an accelerating voltage of 20 kV. Maps of C, N, O, Na, Mg, Si, S, Cl, and K were selected based on the high abundance of these elements in the sample.[19] Additional details of SEM/EDX particle analysis are found elsewhere.[9]

Data Processing. After data acquisition, the ASCII formatted "stack" of STXM images (.xim) and STXM header file (.hdr) is imported into MATLAB™ for further data processing and analysis. A processing routine first aligns[31] the images to correct for image drift encountered during data acquisition. Particle contours within the image are identified using Otsu's method.[32] This method locates the particle contour by separating the image pixels into background and sample classes based on their intensity; the separation threshold is determined to be that which minimizes the intra-class variance. All pixels below the threshold set by Otsu's method are taken to be the regions yielding the intensity transmitted through the particle *(I)*. The particle-free image pixels yield the background intensity (I_0). The aligned "stack" of images is then converted to optical density (OD or absorbance) using the relation $OD = -\ln(I/I_0)$ and saved as MATLAB™ binary files (.mat) for further analysis. This process has been fully automated and scripts are available at http://www.mathworks.com/matlabcentral/fileexchange/24006. These scripts can be used for

applications where statistical approaches are needed, such as engineered and environmental nanoparticles or modified for other absorption edges. Furthermore, a graphical user interface is provided for data exploration. Routines for performing singular value decomposition (SVD), principal components analysis (PCA) and clustering are included. For performing positive matrix factorization (PMF),[33] the program "PMF2" was utilized using FPEAK=-1.5; standard deviations for each pixel were taken to be the standard deviation of its first 10 pre-edge energy points. Particle-free regions were excluded from the PMF analysis.

For processing, the SEM/EDX elemental maps were first converted into binary images using Otsu's method and subsequently noise-filtered. For the S + O map, the pixels were intersected to produce a combined map. After grouping, all binary maps were exported to Photoshop™ and individual colors assigned for each of the elemental maps. An image containing the combined set of elemental maps with 80-90% opacity applied to each map was created and overlaid on the secondary electron microscopy image.

Results

Basic features of Carbon K-edge Spectrum. A typical single particle carbon K-edge (transition from the 1s orbital) near edge X-ray absorption fine structure (NEXAFS) spectrum (Figure 2) contains contributions from several components common in atmospheric particles. The optical density from 278 - 283 eV is known as the pre-edge (OD_{pre}). For typical atmospheric particles the pre-edge offset is mainly due to off-resonance absorption by inorganic elements other than carbon.[34] The post-edge region at 320 eV (OD_{post}) contains contributions from both carbonaceous and non-carbonaceous atoms. The near-edge region, which arises from absorption by carbon 1s transitions, contains several peaks of potential interest between 285 and 290 eV. Here, we focus on the most prominent and unambiguous peaks. The peak at 285.4 eV is due to the characteristic transition (C 1s $\rightarrow \pi^*_{C=C}$; * represents the excited state) of sp^2 hybridized carbon (doubly bonded carbon), labeled $OD_{C=C}$. Since the C 1s $\rightarrow \pi^*_{C=C}$ peak is abundant for soot or elemental carbon (EC),[35] it can be used to identify soot as

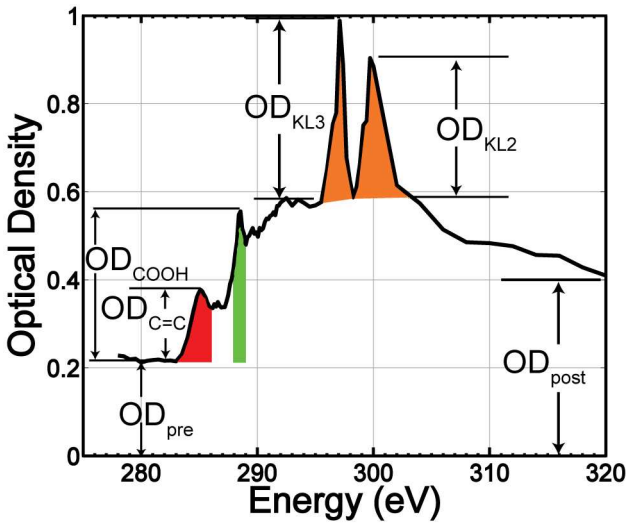

Figure 2. Characteristic single particle carbon K-edge near edge X-ray fine structure (NEXAFS) and spectral feature assignments: "pre-edge" (OD_{pre}) occurs between 278 and 283 eV, carbon-carbon double bonds ($OD_{C=C}$) shown in red, carboxylic acids (OD_{COOH}) shown in green, potassium L_2 and L_3 edges (OD_{KL3}, OD_{KL2}) shown in orange. OD_{post} is the post absorption edge at 320 eV.

described in detail below. The second peak of interest, at 288.5 eV, is characteristic of the C 1s → $\pi^*_{R(C^*=O)OH}$ transition for COOH groups (OD_{COOH}), which are often abundant in atmospheric organic particles.[20,23,36] Therefore, organic constituents are identified by the 288.5 eV peak. A distinct carbonate peak (not shown in Figure 2), often present in dust and sea salt, is observed at 290.4 eV. Finally, the two peaks shaded orange (Figure 2) correspond to the L_2 and L_3 edges of potassium (labeled OD_{KL2} and OD_{KL3}). Potassium in carbonaceous particles is usually apportioned to mineral dust or biomass burning emissions (e.g. biofuel, cooking, wildfires etc.).[37,38]

Figure 3 shows corresponding maps of the four components identified in Figure 2. To reduce noise, pixels less than three times the standard deviation of the pre-edge background are set to zero. OD_{pre} is proportional to the number of non-carbon atoms and OD_{post}-OD_{pre} is proportional to the number of carbon atoms.[34] Hence, the ratio OD_{pre}/OD_{post} can be an indicator of inorganic ("In") material in individual particles. The exact relationship between OD_{pre}/OD_{post} is quantitatively explored below for a variety of inorganic species. In the map of OD_{pre}/OD_{post} shown in Figure 3, the regions of high OD_{pre}/OD_{post} are characterized by compact objects, with the largest ratio occurring in the particle centers.

Potassium peak intensities (OD_{KL2} and OD_{KL3}) were quantified after subtracting the carbon contribution from the spectra. Two straight lines beneath the potassium peaks were calculated using energies between 294 to 295 eV and 302 to 305 eV. The values of these lines at the energy positions of the two potassium peaks were subtracted from the total peak height, giving the quantities OD_{KL2} and OD_{KL3}; these quantities are indicated schematically by heights of the orange peaks in Figure 2. The quantity reported for the "K" component map in Figure 3 is a sum of OD_{KL2} and OD_{KL3}.

The spatial distribution of carbon-carbon double bonds is shown in the % sp^2 map (Figure 3). Employing the procedure of Hopkins et al.[22] the % sp^2 hybridization at each pixel was calculated:

$$\%sp^2 = \left(\frac{A^{Sample}_{C=C}}{A^{Sample}_{280-320}}\right)\left(\frac{A^{HOPG}_{280-320}}{A^{HOPG}_{C=C}}\right)\cdot 100\,.$$

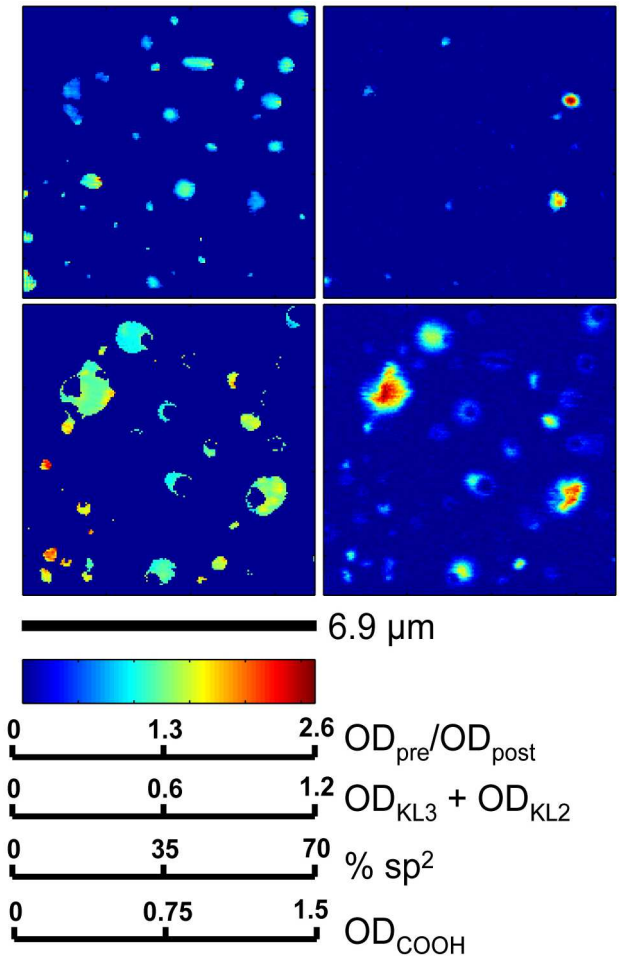

Figure 3. STXM particle maps indicating different spectral components identified in Fig 2: ODpre/ODpost represents total carbon absorption, ODKL3 + ODKL2 is a potassium map (orange peaks in Figure 2), % sp2 shows carbon-carbon double bonds (red peak in Figure 2) and ODCOOH is a map of carboxylic acid groups (green peak in Figure 2).

$A_{C=C}^{Sample}$ is the area of the C 1s → π*$_{C=C}$ peak (285.4 eV) and $A_{280-320}^{Sample}$ is the total area of the carbon K-edge spectrum. $A_{C=C}^{HOPG}$ is the total area of carbon K-edge spectrum for highly oriented polycrystalline graphite (HOPG) and $A_{280-320}^{HOPG}$ the area of the C 1s → π*$_{C=C}$ peak for HOPG reported by Lenardi et al.[39] HOPG is assumed to contain 100% sp^2 hybridized bonds. The resulting % sp^2 map (Figure 3) indicates distinct particle regions that are rich in sp^2 or C=C bonds. While some of the sp^2 rich regions are non-spherical or compact as expected for atmospheric soot particles, several regions are on the periphery coating of the particles, which is indicative of organic carbon. Most of these coatings have lower % sp^2 values than the soot particles. In the next section, this information is employed to identify soot inclusions.

The C 1s → π*$_{R(C*=O)OH}$ transition was used to map particle regions containing organic material. The organic carbon (OC) map (Figure 3 lower right hand panel) is based on the height of the baseline-subtracted carboxylic acid peak (OD_{COOH}-OD_{pre}). The C 1s → π*$_{R(C*=O)OH}$ transition provided the best contrast for organic carbon due to its prominence in the NEXAFS spectrum shown in Figure 2. Based on Figure 3, we surmise that organic material normally coats inorganic-rich regions. This is consistent with organic material from the gas phase condensing onto existing particles.

Component Detection Thresholds for Mixing State Determination. A crucial step in statistically analyzing internally-mixed particles is identifying the entire particle and specific components within each particle that define the mixing state. Figure 4 shows component binary maps produced by identifying species above the detection thresholds defined in this section. The total particle area (Figure 4, lower right) was automatically compared to each component binary map to associate the component with each particle. If a portion of a component map overlapped with the particle area then the particle was assigned the label for that component. For example, in the bottom panels of Figure 4, particle #34 was labeled as InKECOC and particle #37 was labeled as InOC. This labeling procedure was used to report particle type number fractions in Mexico City samples.[19] Hence, it is critical that the

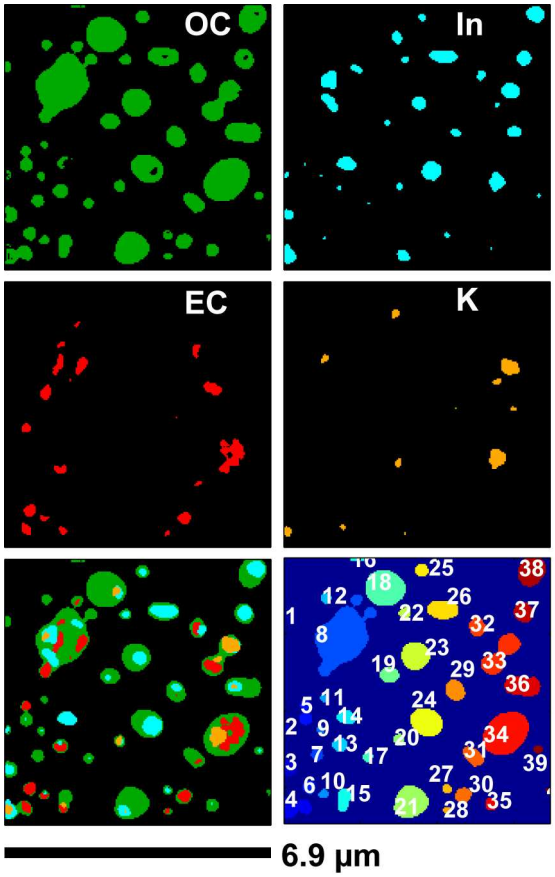

Figure 4. Binary component maps after applying a threshold for organic carbon (OC), inorganic (In) constituents, elemental carbon (EC, or soot), and potassium (K) containing salts. The lower left panel shows the total mixed particle composition with images overlaid in the following order 1) OC, 2) In 3) K 4) EC. The lower right panel shows particle identification indices. From the combined map, particle mixing states are identified. For example, particle #12 is identified as OC, #34 as InKECOC, #38 as InOC, and # 37 as InOC.

thresholds used to produce the binary images shown in Figure 4 are quantitative and reproducible. Therefore, the threshold definitions are detailed below.

To obtain the total particle area, an image of the average OD at each pixel between 288 and 295 eV is obtained. By raising the OD for each pixel in the resulting image to the power of 0.2, the contrast of thin particle coatings or residues are accentuated. Subsequently, Otsu's method is applied to calculate a threshold for producing a binary map of the particle areas. The lower right-hand panel of Figure 4 illustrates an example of the resulting particle areas identified using this procedure.

To identify the organic component, Otsu's method is applied to the contrast-adjusted OD_{COOH}-OD_{pre} map in Figure 3. The detection threshold from Otsu's method is then used to produce the binary map shown in Figure 4. For the In, K and EC components (Figure 3), fixed thresholds were used to produce binary maps as described below.

Elemental carbon (EC, or soot) regions of the samples are identified based on a fixed % sp^2 value of 35%. This value was determined empirically from the observation that the organic carbon rings surrounding the particles disappeared at or above the threshold level (Figure S-1).[5] Only compact and non-spherical inclusions remain in the maps with thresholds at or above 35% sp^2 (Figure 4), which is consistent with previous observations of soot morphology.[40] Furthermore, spectra from pixels below the threshold level more closely resemble organic carbon (Figure S-1).

As noted previously, OD_{pre}/OD_{post} is an indicator of non-carbonaceous constituents in the particle. This is because OD_{pre} is proportional to the number of non-carbon atoms and OD_{post} - OD_{pre} is proportional to the number of carbon atoms.[34] Figure 5A is a spectrum calculated from the atomic cross sections of adipic acid and NaCl. Figure 5A demonstrates the contribution of the inorganic species (e.g. Cl) to OD_{pre} and the contribution of carbon to OD_{post}. A more quantitative interpretation of the pre-to-post edge ratio can be determined with the Beer-Lambert law. The OD of an arbitrary chemical species is

$$OD = -\ln\left(\frac{I}{I_0}\right) = \mu(E)\rho t \qquad (1)$$

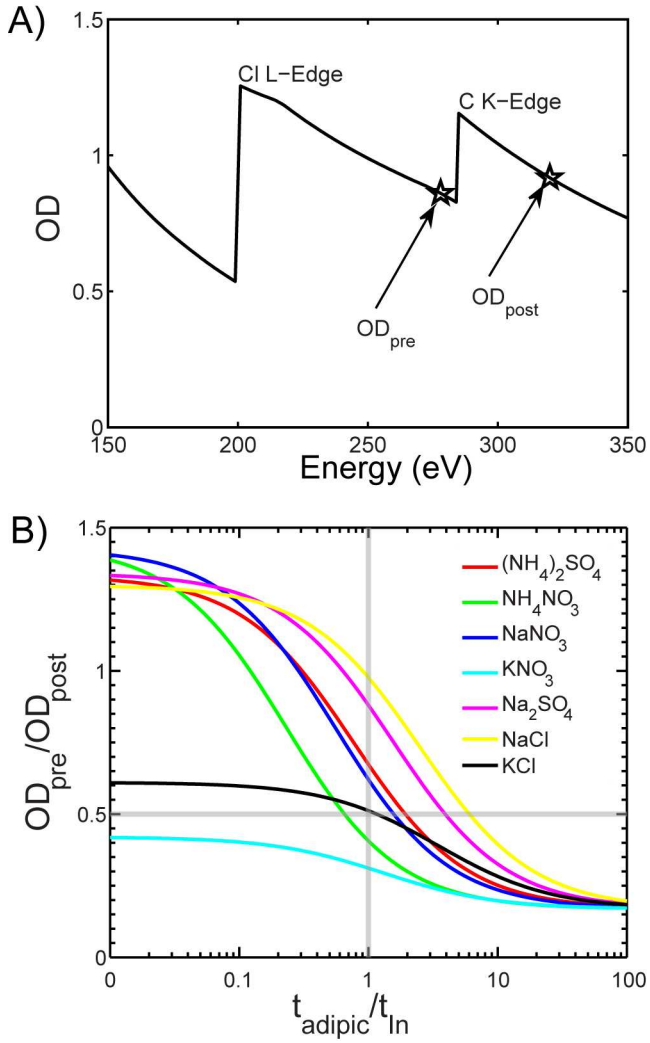

Figure 5. A) Calculated atomic absorption from a mixture of adipic acid and NaCl (each 100 nm thick). The absorption below 150 eV is primarily due to the Na-L edges. B) Calculated pre-edge to post-edge ratios (ODpre/ODpost) as a function of the thickness ratio between adipic acid and inorganic salts common in atmospheric aerosols. For the In map in Figure 4, a threshold of ODpre/ODpost > 0.5 was used to identify inorganic inclusions.

where ρ is the mass density of the material, t is the sample thickness and μ is the mass absorption coefficient. For a chemical compound containing x_i atoms of element i that have an atomic number Z_i, the mass absorption coefficient at energy E can be calculated as:

$$\mu(E) = \frac{\sum_i Z_i x_i \mu(E)_i}{\sum_i x_i Z_i} \quad (2)$$

Typical atmospheric organic particulate matter has an atomic oxygen-to-carbon ratio of about 0.5.[41] Here, the dicarboxylic acid, adipic acid (hexanedioic acid $(CH_2)_4(COOH)_2$, with an atomic ratio O/C = 0.67 and ρ = 1.36 g/cm^3) is used as a proxy for organic particulate matter. Using Equations 1 and 2 for a particle containing a mixture of adipic acid and an inorganic salt ("In"), the pre-to-post edge ratio is expressed in terms of the thickness ratio (t_{adipic}/t_{In}):

$$\frac{OD_{pre}}{OD_{post}} = \frac{\mu_{adipic}(278\ eV)\rho_{adipic}\frac{t_{adipic}}{t_{In}} + \mu_{In}(278\ eV)\rho_{In}}{\mu_{adipic}(320\ eV)\rho_{adipic}\frac{t_{adipic}}{t_{In}} + \mu_{In}(320\ eV)\rho_{In}} \quad (3)$$

The term $\mu_{adipic}(278\ eV)\rho_{adipic}$ is about an order of magnitude smaller than $\mu_{In}(278\ eV)\rho_{In}$ for common atmospheric inorganic salts.

Figure 5B shows the OD_{pre}/OD_{post} ratios calculated as a function of the t_{adipic}/t_{In} thickness ratios for several mixtures of adipic acid and inorganic salt using eq. 3. Atomic scattering is neglected because it is roughly three orders of magnitude smaller than absorption at these energies.[42] These trends hold for a variety of metal and aluminosilicate compounds (Figure S-2). Because potassium salts have an ionization edge over a similar energy range as carbon, $OD_{pre}/OD_{post} < 1$ for all mixtures of potassium salts and organics (Figures 5B, S-3); Pb compounds have the same characteristic (Figure S-2). For pure inorganic salts ($t_{adipic}/t_{In} = 0$), OD_{pre}/OD_{post}~1.3 and is an indicator of the slope of the absorption tail due to the inorganic species (Figure 5A). For thick organic coatings ($t_{adipic}/t_{In} > 1$), OD_{pre}/OD_{post} converges to a value of 0.19. Generally, as the organic O:C atomic ratio increases, OD_{pre}/OD_{post} also increases (Figure

S-2). For example, graphite (O:C = 0) OD_{pre}/OD_{post} = 0.06, glucose (O:C = 1) OD_{pre}/OD_{post} = 0.24 and oxalic acid (O:C = 2) OD_{pre}/OD_{post} = 0.36. As a result, highly oxidized organic particles provide more sensitive detection of inorganic species (Figure S-3). Most importantly, most mixed particles with a pre-edge to post-edge ratio above 0.5 have compositions (on a thickness basis) dominated by inorganic material (Figures 5B and S-3).

Based on this analysis, the threshold for mapping inorganic (In) content was set at OD_{pre}/OD_{post} = 0.5. From the mixed component map (Figure 4), it is seen that the inorganic regions (blue areas) appear as inclusions surrounded by an organic coating (green areas). Comparing maps in Figures 3 and 4, it is apparent that the amount of COOH at the inorganic inclusions is lower than the surrounding particle regions. The threshold value of 0.5 was tested on a variety of different particle samples: carbonaceous urban particles from Mexico City,[19] sea salt coated with organics, and a variety of mineral dust particles. For each of these samples, the inorganic region was accurately mapped using the threshold value of OD_{pre}/OD_{post} = 0.5.

Figure 6A shows OD_{pre}/OD_{post} for a sea salt particle. As expected, areas corresponding to cubic NaCl indicate a high OD_{pre}/OD_{post} ratio. In fact, the majority of the area of the cubic NaCl particle has an OD_{pre}/OD_{post} ratio ~ 1.3, which corresponds to pure NaCl (Figure 5). This is consistent with Figure 3, where the majority of the particles also have a maximum OD_{pre}/OD_{post} ratio of ~ 1.3. For pure NaCl, the value of OD_{pre}/OD_{post} arises from the negatively sloped absorption edge tail from Na and Cl atoms (Figure 5A). Figure 6B shows regions containing inorganic material determined by setting the threshold value of $OD_{pre}/OD_{post} > 0.5$. It is immediately apparent that not only is the cubic NaCl mapped, but also the coating surrounding the NaCl crystal. Figures 6C and 6D show that this coating contains CO_3 and COOH. It should be noted that for thick particles such as the center of the cubic NaCl particle in Figure 4, organic identification can be problematic due to non-linearities. Nevertheless, CO_3 was mapped using a methodology similar to that used for potassium but over the energy range suitable for CO_3. The overlap of CO_3 with the inorganic regions (Figures 6B and 6C), provides further confirmation of the

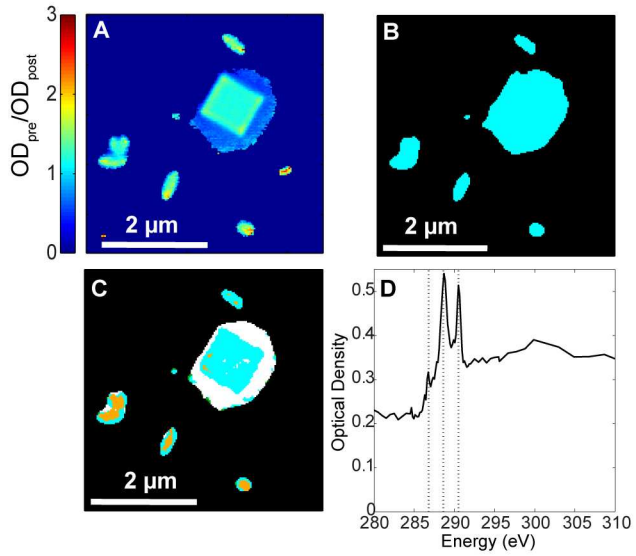

Figure 6. STXM/NEXAFS maps of a sea salt particle: A) the pre edge to post edge ratio (ODpre/ODpost). Values of ODpre/ODpost are depicted by the color scale., B) binary map of areas having ODpre/ODpost> 0.4 C) binary component map showing potassium (orange), inorganic areas (blue), CO3 (white) and organics (green, not visible as displayed). Panel D shows the spectrum taken over the regions containing CO3 and organics.

threshold level for "In" identification. Therefore, the OD_{pre}/OD_{post} threshold of 0.5 appears robust for identifying inorganic inclusions in mixed atmospheric particles.

Comparison with SEM Elemental Maps. To confirm the particle components identified by the STXM mapping procedure at the carbon K-edge, the particles shown in Figures 3 and 4 were subsequently mapped using SEM/EDX. Figure 7 shows a secondary electron (SE) image with elemental maps obtained with SEM/EDX overlaid. The EDX elemental maps provide a detailed elemental picture of the inorganic regions, while the SE image provides a higher resolution view of the carbonaceous component (sum of EC and OC). Comparison of Figure 7 and the particles regions identified by STXM (Figure 4, bottom right) reveals that the smallest (<200 nm) particles in the SE image were not identified as particles using the current STXM mapping routines.

The green transparent color in Figure 7 indicates the carbon rich regions identified by EDX elemental mapping. Comparing Figures 4 and 7, many of the green regions in the SEM/EDX map are associated with both elemental carbon EC and organic carbon (OC) as identified by the STXM. The brighter regions of the secondary electron image that overlap with carbon are particularly rich in elemental carbon as identified by STXM (Figure 4)—these show up as lighter shades of green in Figure 7. The maps for potassium obtained by SEM and STXM, indicated by the orange regions in Figures 7 and 4, are in excellent agreement. Lastly, regions containing sulfur and oxygen in Figure 7 agree well with the inorganic regions identified by the STXM mapping. However, SEM/EDX maps identified fewer inorganic regions than STXM maps. This may be due to beam damage of sensitive inorganic species (such as ammonium sulfate) by either STXM or SEM.

Comparison with other STXM mapping methods. A variety of analysis techniques have been employed to produce chemical maps from STXM data including: clustering,[43] principal component analysis (PCA) coupled with a clustering algorithm,[44] singular value decomposition (SVD),[45] and positive matrix factorization (PMF).[43] Figure 8 demonstrates the application of each of these mapping techniques to the data set used for Figures 3 and 4.

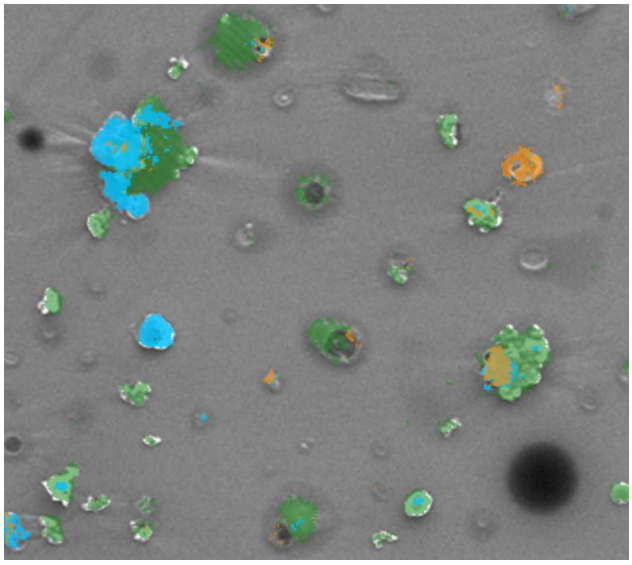

Figure 7. SEM secondary electron image with EDX elemental maps overlaid: C –green, K- orange, S+O – blue.

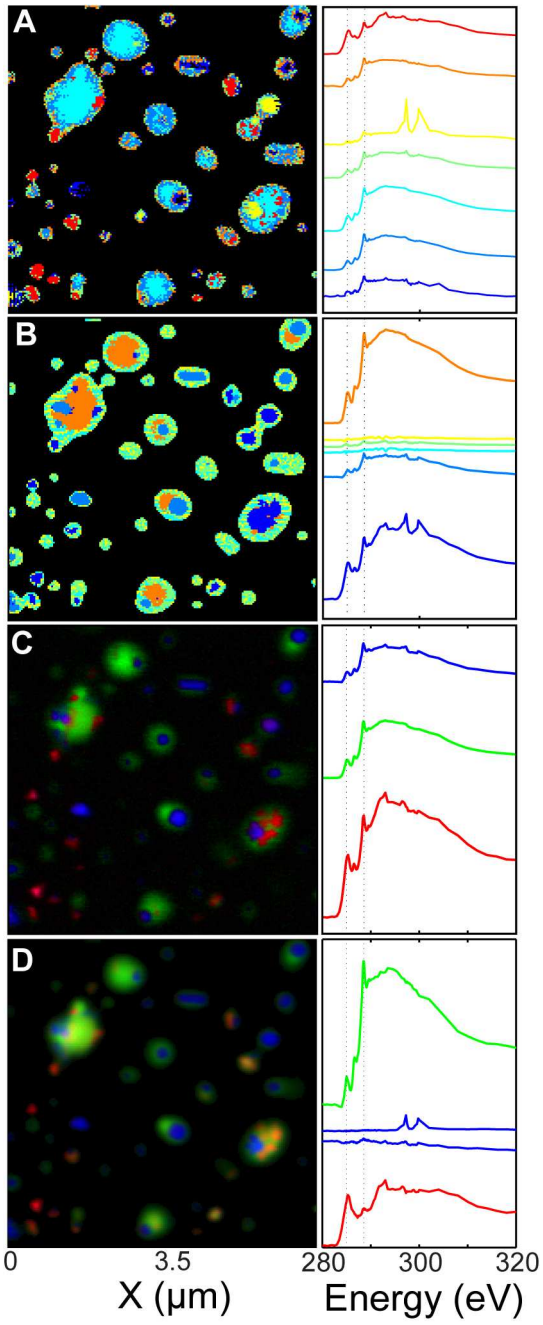

Figure 8. Composition maps (left) and representative spectra (right) at the carbon K-edge derived for the same sample using different mapping methods: A) clustering of particle spectra, B) PCA + clustering, C) SVD using components derived from composition maps, D) PMF. The color of each spectrum corresponds to the same color in the corresponding chemical map (left panels).

Figure 8A shows cluster spectra (right) and a map of their distribution (left) derived using the k-means clustering algorithm. Clustering of spectra results in a binary classification: each pixel is assigned to a single component. Clustering identifies some of the major compositions within the particles (EC, K, OC, In). Notably, clustering identifies differences in the organic component which arise due to the higher relative contribution of the carbon K-edge 1s $\rightarrow \pi^*_{RCOOH}$ and lower total carbon at the thin particle edges. However, some morphological information is lost by displaying the cluster images (compare Figures 7 and 4 with Figure 8A).

Figure 8B shows cluster maps and spectra produced by combining PCA and clustering analysis. The advantage to performing clustering after PCA is that physical spectra are obtained.[44] Furthermore, performing PCA prior to clustering results in much smoother composition maps. However, as with clustering, much of the morphological and optical thickness information is lost with the binary cluster classification. By performing PCA, some aspects of the composition map produced solely by clustering are lost (such as the variations in organic carbon and potassium).

Figure 8C demonstrates the particle composition map derived by performing SVD using spectra provided by the map regions indicated in Figure 4. The SVD map is not a binary classification (as with PCA and/or Clustering) and each pixel has a color intensity that is related to the amount of material present. As expected, the SVD map produces a similar depiction of particle morphology compared to the threshold maps (Figure 4). Furthermore, if the composition is known and carefully calibrated spectra are used in the SVD algorithm, SVD can be mass quantitative.

PMF yields a composition map (Figure 8D) similar to the SVD map. However, the factors derived using PMF more closely resemble pure components. For instance, the EC factor (red) resembles a spectrum of freshly generated flame soot.[22] The PMF results are remarkable because of the limited *a priori* information provided, i.e. 1) the number of factors and 2) a parameter called FPEAK (set at -1.5 for this study). With SVD, the spectra of each component must be provided. In principal, assuming the physical properties of the pure components are known, the PMF composition maps can be mass

quantitative. However, FPEAK and the number of factors needed to produce reasonable (as determined by the experimenter) spectral maps may need to be changed manually, making automation difficult.

One disadvantage of the PMF, SVD, and PCA techniques is that they require *a priori* knowledge about the sample to map components consistently in an automated fashion. Unfortunately, *a priori* knowledge on natural samples or typical environmental particles is usually limited. Information such as the number of factors (chemically distinct components), or other parameters particular to the algorithm will vary from region to region within a sample (as well as among different samples) due to the natural variation in composition. For clustering, relating a set of clusters from one analysis region to another is difficult. Without evaluating these *a priori* assumptions in detail, one cannot be certain of the accuracy of the analysis. This increases the complexity of the analysis and the difficulty of defining particle classes for a statistical analysis.

Conclusion.

The mapping method presented here is a simple, automated way to produce spatial maps of basic components typically found in atmospheric particles. We developed a quantitative mapping technique to identify inorganic material for a statistical analysis. Given that the STXM/NEXAFS technique is element specific, this methodology enables the identification of both inorganic (non-carbonaceous) and organic species at the C K-edge. For EC mapping, the previous approach of using the percentage of sp^2 hybridized bonds was employed.[22] The identification of OC, EC and inorganic regions of particles was confirmed using SEM/EDX. The simplicity of the method described here makes automated analysis facile, significantly reduces analysis time and human bias while comparing different particle samples. Such a detailed, automated comparison cannot be obtained using other methods requiring *a priori* information such as PMF, PCA or clustering. This automated method was recently used to analyze differences in over 1000 particles collected at different times and locations in Mexico City to examine the effects of atmospheric aging on internally mixed atmospheric aerosol particles.[19]

In general, environmental particles are complex mixtures containing variable amounts of (often unknown) organic and inorganic species. The molecular complexity of organic aerosol leads to

additional challenges and requires simplification of the image region under study. Furthermore, the spatial mixing of EC with other components affects their optical properties and potentially influences global climate.[46] Therefore, it is necessary to isolate the regions within individual particles for detailed analysis and modeling of single particle optical properties. The technique presented in this manuscript allows effective isolation of distinctive regions within multi-component particles. Individual, internally mixed particles may be spatially analyzed and the results combined with other particles analyzed the same manner for a statistical representation of the particle population. This spatially resolved approach to single-particle analysis can readily be applied to problems related to climate change, e.g. morphological effects on optical properties or effects of mixed organic-inorganic particles on cloud formation and hygroscopic growth. More broadly, this approach is also suitable for environmental systems such as soil samples, meteorites, or biological samples where statistically significant results are desired for meaningful interpretation rather than extremely detailed results on a single particle or sample.

Acknowledgments. The authors gratefully acknowledge financial support provided by the Atmospheric Science Program of the Department of Energy's office of Biological and Environmental Research. R. C. Moffet acknowledges additional financial support from a Lawrence Berkeley National Laboratory Seaborg Fellowship. The STXM/NEXAFS particle analysis was performed at beamlines 11.0.2 and 5.3.2 at the Advanced Light Source at Lawrence Berkeley National Laboratory. Graduate student Meagan Moore and Prof. Kim Prather at U.C. San Diego are gratefully acknowledged for preparing the sea salt sample. The assistance and support of T. Tyliszczak and A. L. D. Kilcoyne with these instruments is greatly appreciated. The work at the Advanced Light Source was supported by the Director, Office of Science, Office of Basic Energy Sciences, of the U.S. Department of Energy under Contract No. DE-AC02-05CH11231. The SEM/EDX particle analysis was performed in the Environmental Molecular Sciences Laboratory, a national scientific user facility sponsored by the Department of Energy's Office of Biological and Environmental Research at Pacific Northwest National Laboratory. PNNL is operated by the U.S. Department of Energy by Battelle Memorial Institute under

contract DE-AC06-76RL0. T. R. H. acknowledges the student exchange program between the University of Würzburg and U. C. Berkeley (curator Professor A. Forchel, Würzburg and NSF IGERT program at UCB, DGE-0333455, Nanoscale Science and Engineering--From Building Blocks to Functional Systems).

Supporting Information Available: This material is available free of charge via the Internet at http://pubs.acs.org.

References:

(1) IPCC "Climate Change 2007: The Physical Science Basis," Cambridge University Press, 2007.

(2) Pope, C. A.; Ezzati, M.; Dockery, D. W. *New England Journal of Medicine* **2009**, *360*, 376.

(3) Wang, K. C.; Dickinson, R. E.; Liang, S. L. *Science* **2009**, *323*, 1468.

(4) Laskin, A. Electron Beam Analysis and Microscopy of Individual Particles. In *Fundamentals and Applications in Aerosol Spectroscopy*; Signorell, R., Reid, J., Ed.; Taylor and Francis Books, Inc., 2010.

(5) Moffet, R. C.; Tivanski, A. V.; Gilles, M. K. Scanning X-ray Transmission Microscopy: Applications in Atmospheric Aerosol Research. In *Fundamentals and Applications in Aerosol Spectroscopy*; Signorell, R., Reid, J. P., Eds.; Taylor and Francis Books, Inc., 2010.

(6) *Advanced Minerology*; Buseck, P. R.; Anderson, J. R., Eds.; Springer-Verlag: Berlin, 1998; Vol. 3.

(7) *Analytical Chemistry of Aerosols*; De Bock, L. A.; Van Grieken, R. E., Eds.; Lewis Publishers: Boca Raton, FL, 1999.

(8) *Aerosol Measurement*; Fletcher, R. A.; Small, J. A.; Scott, J. H. J., Eds.; John Wiley & Sons: New York, 2001.

(9) Laskin, A.; Cowin, J. P.; Iedema, M. J. *J. Electron Spectrosc. Relat. Phenom.* **2006**, *150*, 260.

(10) Yeung, M. C.; Lee, A. K. Y.; Chan, C. K. *Aerosol Sci. Technol.* **2009**, *43*, 387.

(11) Liu, Y.; Yang, Z. W.; Desyaterik, Y.; Gassman, P. L.; Wang, H.; Laskin, A.; Kim, S. J.; Han, J. *Anal. Chem.* **2008**, *80*, 7179.

(12) Liu, Y.; Laskin, A. *Journal of Physical Chemistry A* **2009**, *113*, 1531.

(13) Ivleva, N. P.; Messerer, A.; Yang, X.; Niessner, R.; Poschl, U. *Environ. Sci. Technol.* **2007**, *41*, 3702.

(14) Ivleva, N. P.; McKeon, U.; Niessner, R.; Poschl, U. *Aerosol Sci. Technol.* **2007**, *41*, 655.

(15) Navratil, M.; Mabbott, G. A.; Arriaga, E. A. *Anal. Chem.* **2006**, *78*, 4005.

(16) Ryu, J.; Ro, C. U. *Anal. Chem.* **2009**, *81*, 6695.

(17) Worobiec, A.; Potgieter-Vermaak, S.; Brooker, A.; Darchuk, L.; Stefaniak, E.; Van Grieken, R. *Microchem. J.* **2010**, *94*, 65.

(18) Maria, S. F.; Russell, L. M.; Gilles, M. K.; Myneni, S. C. B. *Science* **2004**, *306*, 1921.

(19) Moffet, R. C.; Henn, T. R.; Tivanski, A. V.; Hopkins, R. J.; Desyaterik, Y.; Kilcoyne, A. L. D.; Tyliszczak, T.; Fast, J.; Barnard, J.; Shutthanandan, V.; Cliff, S. S.; Perry, K. D.; Laskin, A.; Gilles, M. K. *Atmos. Chem. Phys.* **2010**, *10*, 961.

(20) Russell, L. M.; Maria, S. F.; Myneni, S. C. B. *Geophys. Res. Lett.* **2002**, *29*, doi:10.1029/2002GL014874.

(21) Hopkins, R. J.; Lewis, K.; Desyaterik, Y.; Wang, Z.; Tivanski, A. V.; Arnott, W. P.; Laskin, A.; Gilles, M. K. *Geophys. Res. Lett.* **2007**, *34*, doi:10.1029/2007GL030502.

(22) Hopkins, R. J.; Tivanski, A. V.; Marten, B. D.; Gilles, M. K. *J. Aerosol Sci.* **2007**, *38*, 573.

(23) Tivanski, A. V.; Hopkins, R. J.; Tyliszcazak, T.; Gilles, M. K. *J. Phys. Chem. A* **2007**, *111*, 5448.

(24) Moffet, R. C.; Desyaterik, Y.; Hopkins, R. J.; Tivanski, A. V.; Gilles, M. K.; Wang, Y.; Shutthanandan, V.; Molina, L. T.; Abraham, R. G.; Johnson, K. S.; Mugica, V.; Molina, M. J.; Laskin, A.; Prather, K. A. *Environ. Sci. Technol.* **2008**, *42*, 7091.

(25) Takahama, S.; Gilardoni, S.; Russell, L. M. *J. Geophys. Res.-Atmos.* **2008**, *113*, doi:10.1029/2008JD009810.

(26) Hopkins, R. J.; Desyaterik, Y.; Tivanski, A. V.; Zaveri, R. A.; Berkowitz, C. M.; Tyliszczak, T.; Gilles, M. K.; Laskin, A. *J. Geophys. Res.-Atmos.* **2008**, *113*, doi:10.1029/2007JD008954.

(27) Liu, S.; Takahama, S.; Russell, L. M.; Gilardoni, S.; Baumgardner, D. *Atmos. Chem. Phys.* **2009**, *9*, 6849.

(28) Russell, L. M.; Hawkins, L. N.; Frossard, A. A.; Quinn, P. K.; Bates, T. S. *Proc. Natl. Acad. Sci. U. S. A.* **2010**, *107*, 6652.

(29) Laskin, A.; Iedema, M. J.; Cowin, J. P. *Aerosol Sci. Technol.* **2003**, *37*, 246.

(30) Kilcoyne, A. L. D.; Tyliszczak, T.; Steele, W. F.; Fakra, S.; Hitchcock, P.; Franck, K.; Anderson, E.; Harteneck, B.; Rightor, E. G.; Mitchell, G. E.; Hitchcock, A. P.; Yang, L.; Warwick, T.; Ade, H. *J. Synchrotron Radiat.* **2003**, *10*, 125.

(31) Guizar-Sicairos, M.; Thurman, S. T.; Fienup, J. R. *Opt. Lett.* **2008**, *33*, 156.

(32) Otsu, N. *Ieee Transactions on Systems Man and Cybernetics* **1979**, *9*, 62.

(33) Paatero, P.; Tapper, U. *Environmetrics* **1994**, *5*, 111.

(34) Henke, B. L.; Gullikson, E. M.; Davis, J. C. *Atomic Data and Nuclear Data Tables* **1993**, *54*, 181.

(35) Bond, T. C.; Bergstrom, R. W. *Aerosol Sci. Technol.* **2006**, *40*, 27.

(36) Takahama, S.; Gilardoni, S.; Russell, L. M.; Kilcoyne, A. L. D. *Atmos. Environ.* **2007**, *41*, 9435.

(37) Andreae, M. O. *Science* **1983**, *220*, 1148.

(38) Moffet, R. C.; de Foy, B.; Molina, L. T.; Molina, M. J.; Prather, K. A. *Atmos. Chem. Phys.* **2008**, *8*, 4499.

(39) Lenardi, C.; Marino, M.; Barborini, E.; Piseri, P.; Milani, P. *European Physical Journal B* **2005**, *46*, 441.

(40) Posfai, M.; Anderson, J. R.; Buseck, P. R.; Sievering, H. *J. Geophys. Res.-Atmos.* **1999**, *104*, 21685.

(41) Aiken, A. C.; Decarlo, P. F.; Kroll, J. H.; Worsnop, D. R.; Huffman, J. A.; Docherty, K. S.; Ulbrich, I. M.; Mohr, C.; Kimmel, J. R.; Sueper, D.; Sun, Y.; Zhang, Q.; Trimborn, A.; Northway, M.; Ziemann, P. J.; Canagaratna, M. R.; Onasch, T. B.; Alfarra, M. R.; Prevot, A. S. H.; Dommen, J.; Duplissy, J.; Metzger, A.; Baltensperger, U.; Jimenez, J. L. *Environ. Sci. Technol.* **2008**, *42*, 4478.

(42) Hubbell, J. H.; Gimm, H. A.; Overbo, I. *J. Phys. Chem. Ref. Data* **1980**, *9*, 1023.

(43) Takahama, S.; Liu, S.; Russell, L. M. *J. Geophys. Res.-Atmos.* **2010**, *115*.

(44) Lerotic, M.; Jacobsen, C.; Schafer, T.; Vogt, S. *Ultramicroscopy* **2004**, *100*, 35.

(45) Koprinarov, I. N.; Hitchcock, A. P.; McCrory, C. T.; Childs, R. F. *J. Phys. Chem. B* **2002**, *106*, 5358.

(46) Moffet, R. C.; Prather, K. A. *Proc. Natl. Acad. Sci. U. S. A.* **2009**, *106*, 11872.

LEGAL DISCLAIMER